



OPEN

Determination of Dy substitution site in $\text{Nd}_{2-x}\text{Dy}_x\text{Fe}_{14}\text{B}$ by HAADF-STEM and illustration of magnetic anisotropy of “g” and “f” sites, before and after substitution

Syed Kamran Haider^{1,2,3,6}, Min-Chul Kang^{4,6}, Jisang Hong⁵, Young Soo Kang³✉, Cheol-Woong Yang⁴✉ & Dongsoo Kim^{1,2}✉

$\text{Nd}_2\text{Fe}_{14}\text{B}$ and $\text{Nd}_{2-x}\text{Dy}_x\text{Fe}_{14}\text{B}$ ($x = 0.25, 0.50$) particles were prepared by the modified co-precipitation followed by reduction-diffusion process. Bright field scanning transmission electron microscope (BF-STEM) image revealed the formation of Nd–Fe–B trigonal prisms in $[-101]$ viewing zone axis, confirming the formation of $\text{Nd}_2\text{Fe}_{14}\text{B}/\text{Nd}_{2-x}\text{Dy}_x\text{Fe}_{14}\text{B}$. Accurate site for the Dy substitution in $\text{Nd}_2\text{Fe}_{14}\text{B}$ crystal structure was determined as “f” site by using high-angle annular dark field scanning transmission electron microscope (HAADF-STEM). It was found that all the “g” sites are occupied by the Nd, meanwhile Dy occupied only the “f” site. Anti-ferromagnetic coupling at “f” site decreased the magnetic moment values for $\text{Nd}_{1.75}\text{Dy}_{0.25}\text{Fe}_{14}\text{B}$ (23.48 μB) and $\text{Nd}_{1.5}\text{Dy}_{0.5}\text{Fe}_{14}\text{B}$ (21.03 μB) as compared to $\text{Nd}_2\text{Fe}_{14}\text{B}$ (25.50 μB). Reduction of magnetic moment increased the squareness ratio, coercivity and energy product. Analysis of magnetic anisotropy at constant magnetic field confirmed that “f” site substitution did not change the patterns of the anisotropy. Furthermore, magnetic moment of $\text{Nd}_2\text{Fe}_{14}\text{B}$, $\text{Nd}_{2-x}\text{Dy}_x\text{Fe}_{14}\text{B}$, Nd (“f” site), Nd (“g” site) and Dy (“f” site) was recorded for all angles between 0° and 180° .

$\text{Nd}_2\text{Fe}_{14}\text{B}$ type magnets have the highest recorded maximum energy product ($\text{BH})_{\text{max}}$ among permanent magnets^{1–5}. They have drawn huge attention due to their wide applications in wind turbines, hybrid-electric vehicles, transducers, magnetic fluids, magnetic elastomers, sensors, magnetic separators, magnetic levitation systems, loudspeakers, generators and motors^{6–11}. Current maximum coercivity of unsubstituted $\text{Nd}_2\text{Fe}_{14}\text{B}$ is recorded as 10 kOe, which makes it economically inadequate for commercial purpose. However, magnetic properties of $\text{Nd}_2\text{Fe}_{14}\text{B}$ have been improved significantly by the substitution of Nd with rare earth elements (RE)^{12–21}. Hence the synthesis of $\text{Nd}_{2-x}\text{RE}_x\text{Fe}_{14}\text{B}$ by RE substitution for Nd is vital for the applications of $\text{Nd}_2\text{Fe}_{14}\text{B}$ on commercial scale. The site of RE atoms in the $\text{Nd}_{2-x}\text{RE}_x\text{Fe}_{14}\text{B}$ crystal lattice is very critical for its anisotropy and magnetic moment. $\text{Nd}_2\text{Fe}_{14}\text{B}$ is a tetragonal structure with four formula units and 68 atoms, which has two unequal sites for Nd (RE), “g” site and “f” site. When RE substitutes for Nd in $\text{Nd}_2\text{Fe}_{14}\text{B}$ crystal lattice, it may either substitute at “f” or “g” site. Aftab, Kitagawa and Liu et al. have worked to estimate the substitution site for RE in $\text{Nd}_2\text{Fe}_{14}\text{B}$ theoretically, by using density function theory (DFT)^{19–21}. Aftab et al. applied Vienna ab initio simulation package (VASP) with a pseudo-potential and projected-augmented wave (PAW) method. Kitagawa et al. applied the

¹Convergence Research Center for Development of Mineral Resources, Korea Institute of Geoscience and Mineral Resources, Daejeon 34132, South Korea. ²Powder and Ceramics Division, Korea Institute of Materials Science, Changwon, Gyeongnam 51508, South Korea. ³Department of Chemistry, Sogang University, 35, Baekbeomro, Mapo-gu, Seoul 04107, South Korea. ⁴School of Advanced Materials Science and Engineering, Sungkyunkwan University, Suwon 16419, South Korea. ⁵Department of Physics, Pukyong National University, Busan 48513, South Korea. ⁶These authors contributed equally: Syed Kamran Haider and Min-Chul Kang. ✉email: yskang@sogang.ac.kr; cwyang@skku.edu; dskim69@kigam.re.kr

linear combination of pseudo-atomic-orbital (LCPAO) method, while Liu et al. used full potential plane-wave plus muffin-tin orbital method.

Experimental evidences for Dy site in $(\text{Nd}-\text{Dy})_2\text{Fe}_{14}\text{B}$ crystal lattice was provided by Itakura et al.²² Although they presented STEM-HAADF image but d-spacing value for the [001] facet deviated from the standard values. Absence of the stoichiometric ratio between Nd:Dy:Fe and distribution of Dy only near grain boundary raised more questions, hence it was interesting for the contemporary researchers to answer them. Saito et al.²³ used neutron diffraction technique and determined the quantitative distribution of Dy at substitution sites. They postulated that Dy substitutes at both the “f” and “g” sites, and population of Dy on each site depends on the annealing temperature of the experiment. This finding was different from the previous studies, those suggested that Dy only substitutes at “f” site. Furthermore, magnetic anisotropic properties of “f” and “g” sites in $\text{Nd}_{2-x}\text{Dy}_x\text{Fe}_{14}\text{B}$ were not yet studied. In order to answer the questions discussed above and a comprehensive study of “f” and “g” sites in $\text{Nd}_{2-x}\text{Dy}_x\text{Fe}_{14}\text{B}$ was required.

In this work, we prepared $\text{Nd}_2\text{Fe}_{14}\text{B}$ and $\text{Nd}_{2-x}\text{Dy}_x\text{Fe}_{14}\text{B}$ with optimized co-precipitation method followed by reduction-diffusion (R-D) process. This co-precipitation method is similar with the approach reported by Ma and Palaka et al. with minor modification^{24,25}. Detail of this modification is explained in the “supplementary information”. Site preference of Dy in $\text{Nd}_{1.5}\text{RE}_{0.5}\text{Fe}_{14}\text{B}$ particles was confirmed through the crystal structure determination by using HAADF-STEM. Effect of Dy substitution on the magnetic moment, magneto-crystalline anisotropy energy and coercivity of the $\text{Nd}_{2-x}\text{Dy}_x\text{Fe}_{14}\text{B}$ particles is also studied. $\text{Nd}_{2-x}\text{Dy}_x\text{Fe}_{14}\text{B}$ sample was rotated in the rotating angle range of 0° to 180° at the constant magnetic field to observe variation of anisotropic patterns after the substitution. Effect of the substitution on the anisotropic properties of “f” and “g” sites in the $\text{Nd}_{2-x}\text{Dy}_x\text{Fe}_{14}\text{B}$ crystal is also studied.

Methods

Materials. All chemicals used in this work, including neodymium (III) chloride hexahydrate ($\text{NdCl}_3 \cdot 6\text{H}_2\text{O}$), iron (III) chloride hexahydrate ($\text{FeCl}_3 \cdot 6\text{H}_2\text{O}$), sodium hydroxide (NaOH), boric acid (H_3BO_3), calcium hydride (CaH_2), dysprosium (III) chloride hexahydrate ($\text{DyCl}_3 \cdot 6\text{H}_2\text{O}$), ethyl alcohol ($\text{C}_2\text{H}_5\text{OH}$) and acetone (CH_3COCH_3) were analytical grade and obtained from Sigma-Aldrich Co.

Preparation of $\text{Nd}_{1.5}\text{RE}_{0.5}\text{Fe}_{14}\text{B}$ particles. Schematics for the preparation procedure is shown as the Fig. S1 and detailed process of synthesis is explained in the “supplementary information”. In brief, all the metal chlorides of Nd, Fe and Dy were dissolved in deionized (D.I.) water under the stirring to obtain the clear solution. NaOH (3.5 M) was added to the solution in a drop wise until the pH approached to 13. The resultant solution was stirred continuously for 4 h. Then, products were washed twice with D.I. water and ethanol, and dried overnight at 353 K (80°C) followed by annealing at 973.15 K (700°C) for 30 min to convert all hydroxides to oxides. The product was mixed with boric acid and CaH_2 in a glove box and then pressed into pellet form. The pellet was undergone to R-D via annealing at 1273.15 K (1000°C) for 3 h with Ar flowing in the furnace. The pellet after R-D was pulverized and washed with water to remove calcium oxide (CaO) completely and rinsed with acetone. To obtain $\text{Nd}_2\text{Fe}_{14}\text{B}$, weight ratio of Nd:Fe:B was kept as 15:77:8, as per standard ratio for the synthesis of $\text{Nd}_2\text{Fe}_{14}\text{B}$ by R-D. In order to produce $\text{Nd}_{1.75}\text{Dy}_{0.25}\text{Fe}_{14}\text{B}$ and $\text{Nd}_{1.5}\text{RE}_{0.5}\text{Fe}_{14}\text{B}$, Nd:Dy:Fe:B ratio was kept as 13.12:1.88:77:8 and 11.25:3.75:77:8, hence 12.5% and 25% of Nd was substituted with Dy, respectively. Nd:Dy ratios in $\text{Nd}_{1.75}\text{Dy}_{0.25}\text{Fe}_{14}\text{B}$ and $\text{Nd}_{1.5}\text{Dy}_{0.5}\text{Fe}_{14}\text{B}$ were determined as 7.17:1 and 3.13:1 experimentally (Figs. S3, S4). These values were quite close to the theoretically expected ratios of Nd:Dy ratios, 7:1 and 3:1.

Samples preparation for SEM and TEM. $\text{Nd}_2\text{Fe}_{14}\text{B}$ and $\text{Nd}_{2-x}\text{Dy}_x\text{Fe}_{14}\text{B}$ powder samples were placed on the movable lower ram and then the prepared solder pieces were placed on the sample. Electrically conductive polymer was poured to encapsulate the solder and powder samples, then heated at 180°C for 6 min and then pressed under the pressure of 30 kN. Prepared sample was mounted on SEM holder, then mechanically polished with SiC paper, diamond suspension and colloidal silica, subsequently characterized with FE-SEM.

Specimens for TEM (transmission electron microscope) were prepared by focused ion beam (FIB-NX2000, Hitachi) using the lift-out technique. For TEM measurement, sample was treated as the same process reported by Kim et al.²⁶ and orientation of sample along [100] zone axis was confirmed by using electron backscatter diffraction (EBSD) (TEAM™ Pegasus, Ametek Co. Ltd. USA).

Characterization. Crystal structure and phases were determined by X-ray diffraction (XRD) patterns using a Rigaku Diffractometer (XRD, Rigaku). The morphology, size and elemental distribution were observed with field emission scanning electron microscope (JSM-7000F, JEOL), conventional transmission electron microscopy (TEM, JEM-2100F) and aberration corrected TEM (ARM-200F) with energy dispersive X-ray spectroscopy (EDS). TEM was operated at the accelerating voltage of 200 kV. Angular dependent magnetic properties were measured by magnetic property measurement system (MPMS3-Evercool) equipped with rotator. Magnetic properties (M-H curves) of final product were measured by Physical Property Measurement System (PPMS, Evercool II-9 T) in the vibrating sample magnetometer mode. Magnetic field in the range of 7179.3 to -7179 kA/m was applied to measure the magnetic properties of the final products. JEOL JEM-ARM200F Cs-corrected TEM was used to obtain HAADF-STEM images.

Numerical method. Full potential linearized augmented plane wave method, as implemented in the Wien2k code, was used to calculate the magnetic moment of $\text{Nd}_2\text{Fe}_{14}\text{B}$ and $\text{Nd}_{2-x}\text{Dy}_x\text{Fe}_{14}\text{B}$. Details are described in “supplementary information”.

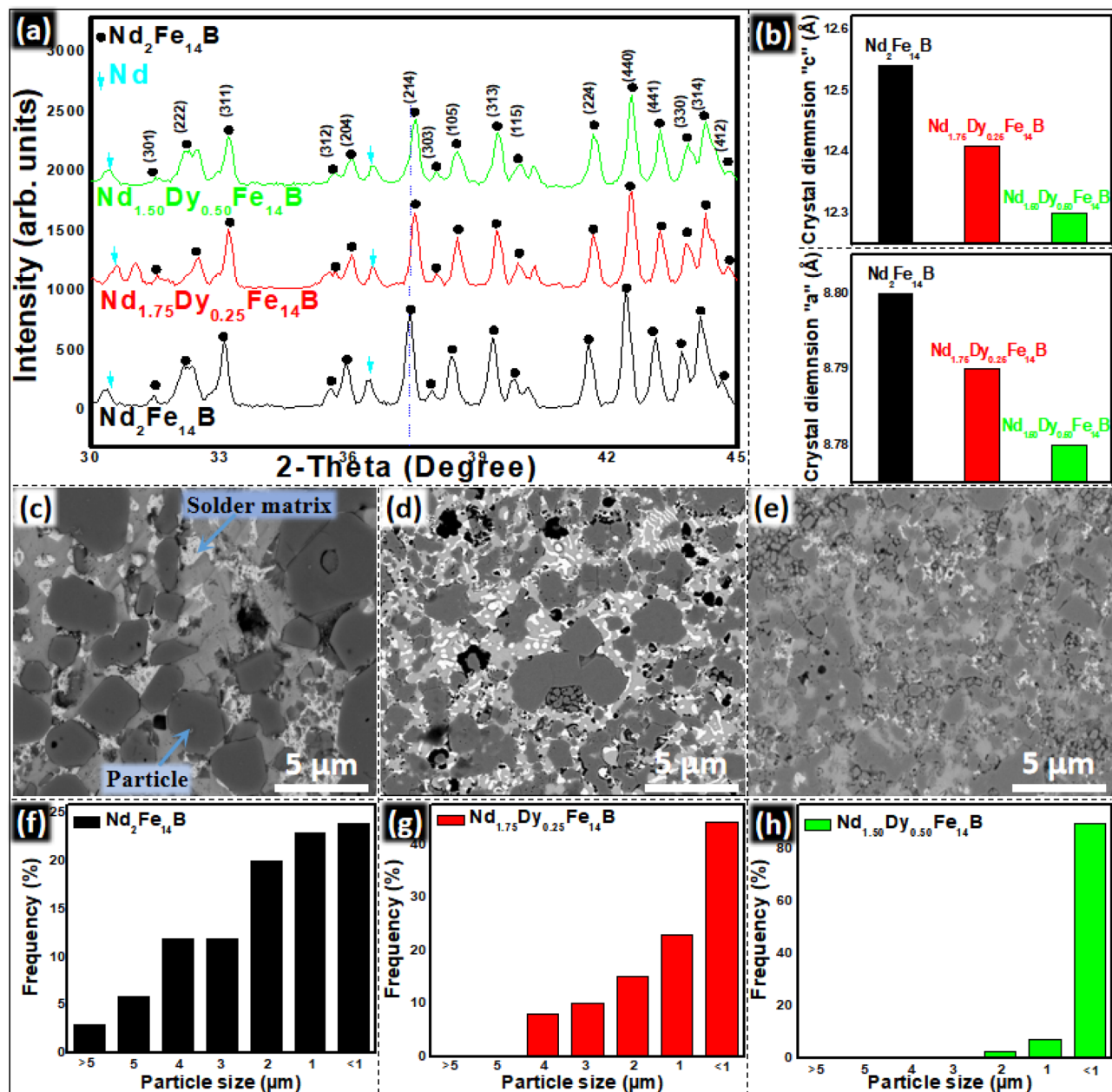


Figure 1. (a) XRD patterns of $\text{Nd}_2\text{Fe}_{14}\text{B}$ and $\text{Nd}_{2-x}\text{Dy}_x\text{Fe}_{14}\text{B}$ particles (b) crystal parameters "a" and "c" of $\text{Nd}_2\text{Fe}_{14}\text{B}$ and $\text{Nd}_{2-x}\text{Dy}_x\text{Fe}_{14}\text{B}$. BSE-SEM images of (c) $\text{Nd}_2\text{Fe}_{14}\text{B}$ (d) $\text{Nd}_{1.75}\text{Dy}_{0.25}\text{Fe}_{14}\text{B}$ and (e) $\text{Nd}_{1.5}\text{Dy}_{0.5}\text{Fe}_{14}\text{B}$ particles. Particle size distribution of (f) $\text{Nd}_2\text{Fe}_{14}\text{B}$ (g) $\text{Nd}_{1.75}\text{Dy}_{0.25}\text{Fe}_{14}\text{B}$ and (h) $\text{Nd}_{1.5}\text{Dy}_{0.5}\text{Fe}_{14}\text{B}$ particles.

Results and discussion

$\text{Nd}_2\text{Fe}_{14}\text{B}$ and $\text{Nd}_{2-x}\text{Dy}_x\text{Fe}_{14}\text{B}$ magnetic particle were prepared by co-precipitation followed by reduction diffusion process. Chemical reactions and mechanisms during co-precipitation and R-D processes are explained in the "supporting information". R-D reaction follows the mechanism proposed by the Haider et al.²⁷ XRD patterns for $\text{Nd}_2\text{Fe}_{14}\text{B}$ and $\text{Nd}_{2-x}\text{Dy}_x\text{Fe}_{14}\text{B}$ particles are similar due to the almost same crystal structure (Fig. 1a). They have the $\text{Nd}_2\text{Fe}_{14}\text{B}$ (JCPDS #36-1296) as main phase with additional peaks corresponding to the extra Nd phase. Nd substitution with Dy makes the peaks position be shifted to the right side (Fig. 1a).

This is due to the different crystal lattice parameters of $\text{Nd}_{2-x}\text{Dy}_x\text{Fe}_{14}\text{B}$ and to the smaller ionic radii of Dy (178 pm) as compared to the Nd (181 pm). Both "a" and "c" dimensions of the crystal lattice were decreased after the Dy substitution in the $\text{Nd}_2\text{Fe}_{14}\text{B}$ crystal lattice (Fig. 1b). The decreased values of these $\text{Nd}_{1.5}\text{RE}_{0.5}\text{Fe}_{14}\text{B}$ crystal parameters are also evidence of Dy substitution in $\text{Nd}_2\text{Fe}_{14}\text{B}$ crystal. In order to calculate the lattice parameters ("a" and "c"), at first d-spacing values were calculated from the XRD patterns (Fig. 1). h, k and l values were determined from $\text{Nd}_2\text{Fe}_{14}\text{B}$ JCPDS #36-1296. Finally, "c" and "a" value were calculated by the following equation as the same method reported by Rahimi¹⁷, Cullity²⁸, and Charbel²⁹, et al.

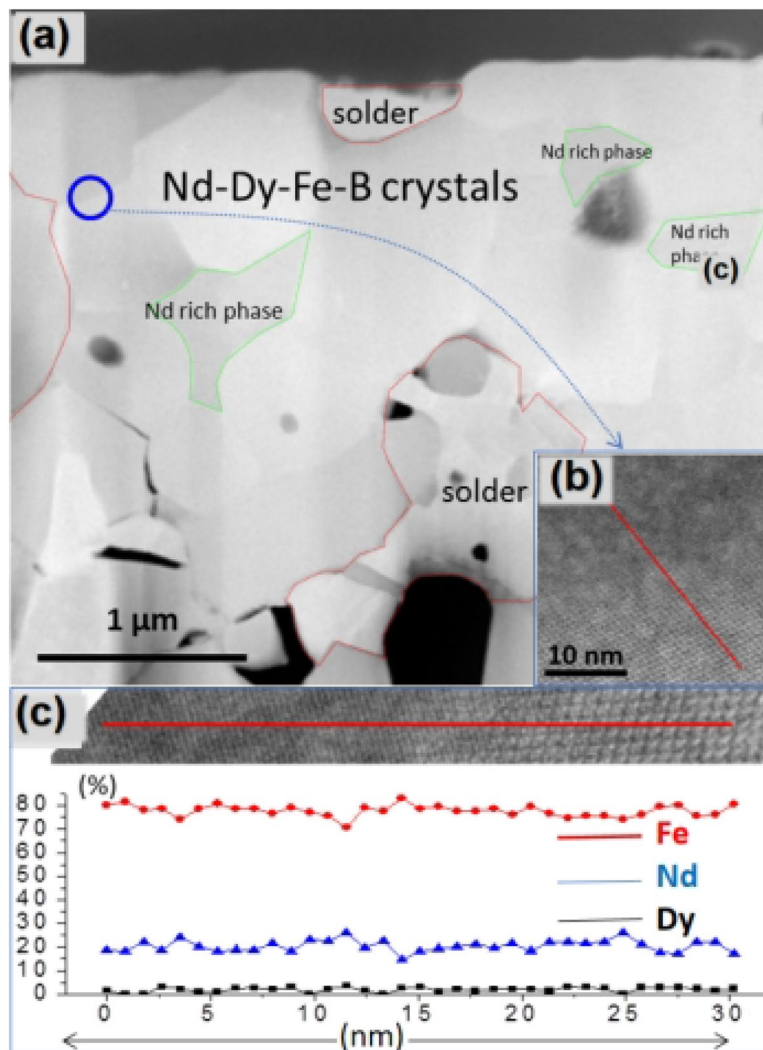


Figure 2. (a) LAADF-STEM image of $\text{Nd}_{1.5}\text{Dy}_{0.5}\text{Fe}_{14}\text{B}$, (b) HAADF-STEM image and corresponding EDS line profile taken from blue circle in (a). (c) EDS line profile of (b).

SEM-BSE images in Fig. 1c–e revealed that the particles were in irregular shape and the size distribution is in the range of 0.3–10 μm . The $\text{Nd}_2\text{Fe}_{14}\text{B}$ had the largest average particle size as 3.5 μm while $\text{Nd}_{1.5}\text{Dy}_{0.5}\text{Fe}_{14}\text{B}$ had the least average particle size as 0.8 μm . $\text{Nd}_{1.75}\text{Dy}_{0.25}\text{Fe}_{14}\text{B}$ had the average particle size of 1.7 μm . SEM-EDS confirmed that Nd and Dy are homogeneously distributed with Fe in the particles (Figs. S5, S6). The microstructure, elemental composition and distribution of $\text{Nd}_{1.5}\text{Dy}_{0.5}\text{Fe}_{14}\text{B}$ particles were evaluated with STEM as shown in Fig. 2. The elemental distribution of Nd, Dy, Fe, and O was investigated by using STEM-EDS, which confirmed that the Dy was substituted for Nd in the crystal structure and it was distributed inside the grain. Figure 2b is the line EDS taken from the blue circle of LAADF-STEM image of $\text{Nd}_{1.5}\text{Dy}_{0.5}\text{Fe}_{14}\text{B}$. Figure 2c shows the EDS line profile of interface between two fused $\text{Nd}_{1.5}\text{Dy}_{0.5}\text{Fe}_{14}\text{B}$ particles, as marked with the blue circle in Fig. 2a. No oxygen was detected in EDS mapping because boundaries of the particles were not exposed to the water during washing process.

To evaluate the crystallinity of the specimen, SAED patterns (Fig. 3b) of the marked area with red circle in the TEM image (Fig. 3a) were obtained. It was confirmed that the particles produced were single crystalline. It was deduced by SAEDP of strong diffraction maxima that each grain was completely single crystalline. Figure 3d shows the high resolution BF-STEM image of the $\text{Nd}_{1.5}\text{Dy}_{0.5}\text{Fe}_{14}\text{B}$ observed at the $[-101]$ zone axis and Fig. 3e represents the corresponding atomic arrangement simulated by JEMS software (P. Stadelmann, www.jems-saas.ch).

Both the BF-STEM image and simulated atomic arrangement showed the series of trigonal prism units. Figure 3c illustrates the arrangement of the atoms in the prism. Boron atom occupies the center of trigonal prisms surrounded with three nearest Fe atoms on top and the three Fe atoms at bottom. The triangular prism facets participate to form the complete tetragonal $\text{Nd}_2\text{Fe}_{14}\text{B}$ lattice.

To know the accurate site of the RE in the crystal lattice, HAADF-STEM image was taken at the $[100]$ zone axis as shown in Fig. 4. At $[100]$ zone axis, columns having “4f” site and “4 g” site of Nd/Dy can be clearly distinguished. In addition, there is no Fe atom overlapping at each Nd position because of different locations of Fe and RE at $[100]$ zone axis. Peak intensity of the histogram increases with the average atomic number, the

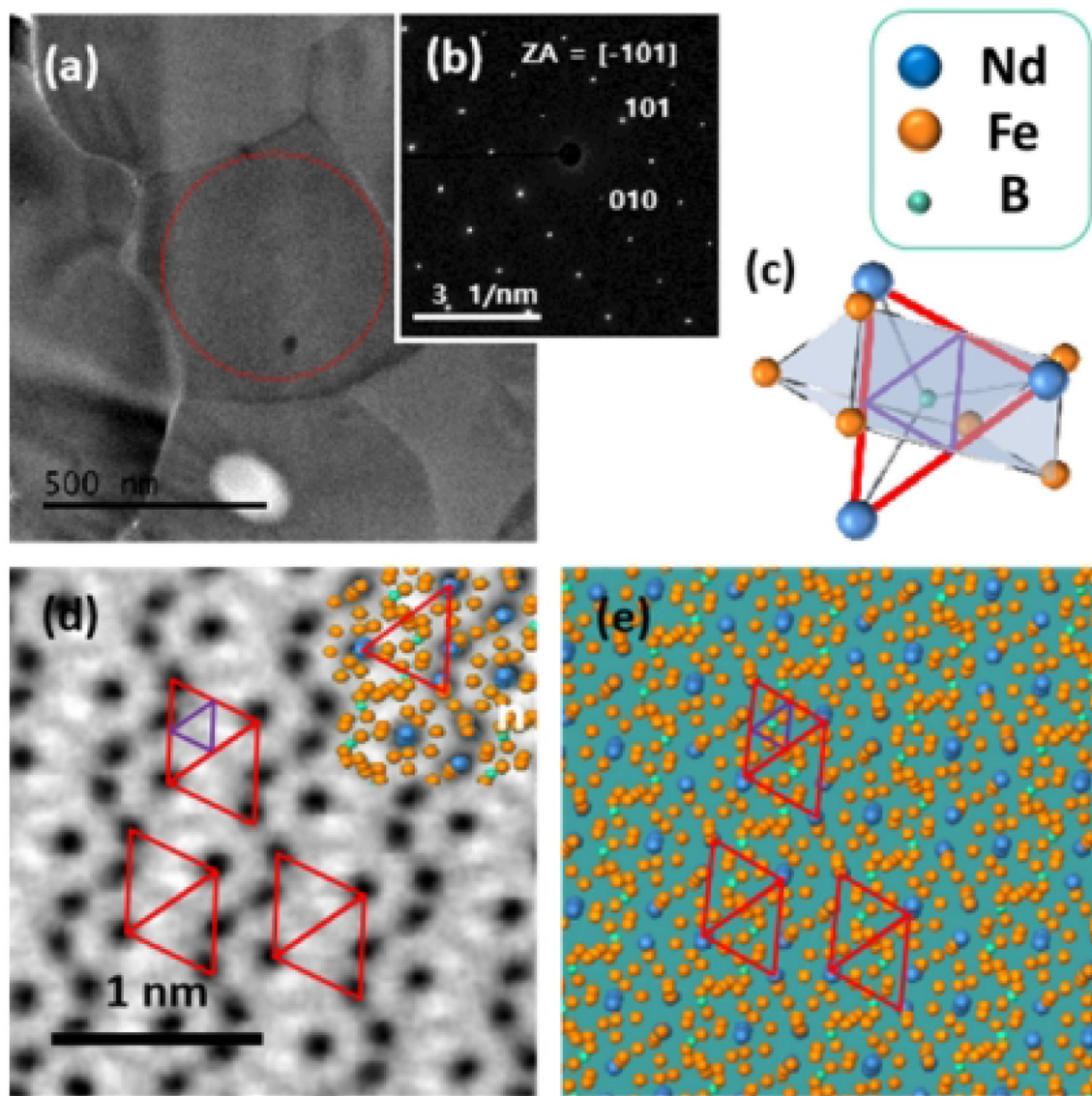


Figure 3. (a) TEM image of the $\text{Nd}_{1.5}\text{Dy}_{0.5}\text{Fe}_{14}\text{B}$, (b) SAED pattern taken from the red circle in (a), (c) $\text{Nd}_2\text{Fe}_{14}\text{B}$ trigonal prism in the $[-101]$ viewing zone axis, (d) high resolution BF-STEM image of $\text{Nd}_{1.5}\text{Dy}_{0.5}\text{Fe}_{14}\text{B}$ at $[-101]$ zone axis and (e) simulation of arrangement of the atoms by JEMS software.

HAADF-STEM image can be used to distinguish the Dy and Nd, and their positions (“f” or “g” site). Figure 4b is HAADF-STEM image, which confirms the same arrangement of atoms as the standard $\text{Nd}_2\text{Fe}_{14}\text{B}$ [100] zone axis (Fig. 3a). Intensity histogram for red dotted panel in Fig. 4b was acquired. It is observed that the intensity of atoms (Dy) at “4f” column is higher than that of the atom (Nd) at “4 g” column. Higher peak intensity confirms that the substitution site of Dy is “4f” site because the atomic number of Dy (66) is larger than that of Nd (60), which leads to the higher intensity as compared to the Nd. The ‘a’ value of $\text{Nd}_{1.5}\text{Dy}_{0.5}\text{Fe}_{14}\text{B}$ crystal lattice is 8.78 Å (Fig. 3c), which is well consistent with the standard $\text{Nd}_{1.5}\text{Dy}_{0.5}\text{Fe}_{14}\text{B}$ value.

Standard $\text{Nd}_2\text{Fe}_{14}\text{B}$ have ‘a’ and ‘b’ values of lattice parameters as 8.80 Å³⁰. Standard distance of atomic column between “4f” site and “4 g” site of $\text{Nd}_2\text{Fe}_{14}\text{B}$ is 1.1 Å. In this study, the obtained distance is 1.09 Å as shown in histogram Fig. 4c. This is well matched with theoretical value. A slight error is due to a noise induced by the fine drift of the sample or the poisson noise in the STEM. Hence, site preference for the Dy in $\text{Nd}_2\text{Fe}_{14}\text{B}$ is proved to be “4f” as the previously theoretically reported by Liu et al.²¹. It was found that 100% “g” sites are occupied by the Nd (Fig. 5) and Dy was substituted only at “f” site.

Fe is ferromagnetic with electronic configuration of $[\text{Ar}] 3d^6 4s^2$. This electronic configuration shows that it has eight valence electrons. Arrangement of the electrons in the relevant orbitals is shown in the rigid band model as Fig. 6c. Density of the electrons was taken on X-axis and energy was taken on Y-axis. E_f indicates the Fermi level of the rigid band. Energy level of 3-d electrons is similar to the 4 s electrons, hence, there is no movement of electrons between the 4s and 3d orbital. Four unpaired electrons will be in the spin up configuration. Presence of the unpaired electrons makes the Fe ferromagnetic.

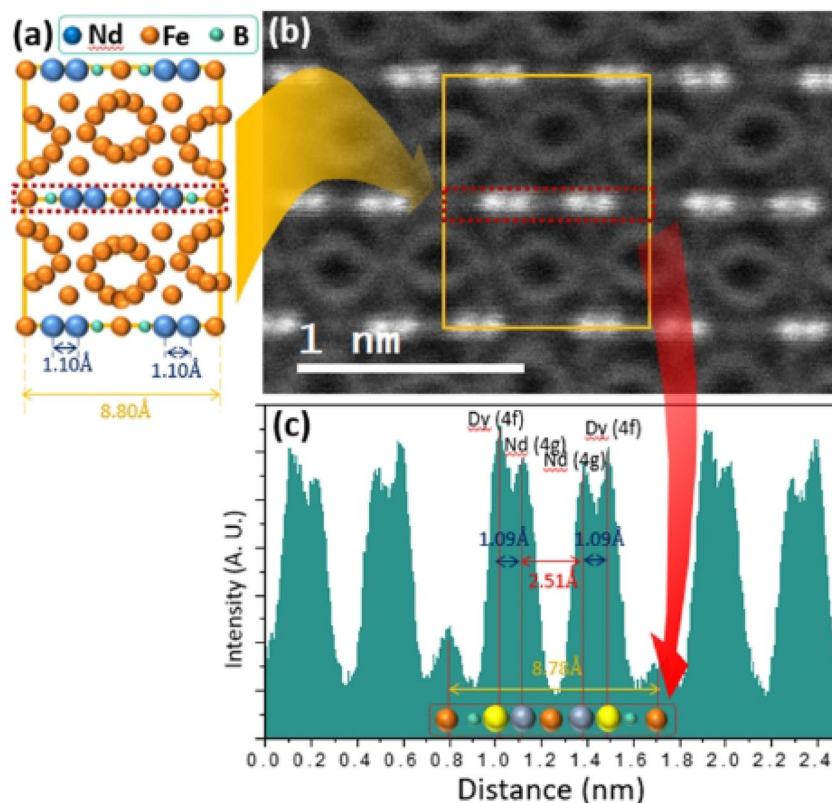


Figure 4. (a) Standard $\text{Nd}_2\text{Fe}_{14}\text{B}$ unit cell with [100] zone axis (b) HADDF-STEM image of $\text{Nd}_{1.5}\text{Dy}_{0.5}\text{Fe}_{14}\text{B}$ at [100] zone axis, (c) intensity histogram for the atoms in the red dotted panel in (b).

Being completely filled, 5d orbitals in Nd or Dy do not play any role to determine the magnetic properties of Nd or Dy. However, Nd and Dy have unpaired electrons in the 4f orbitals, those impart the ferromagnetic character. Orbital magnetic moment (L) direction of the unpaired valence electrons in Dy is opposite to the Nd because 4f electrons in Dy are in spin down state. Nd has the unpaired electrons in the spin up direction, hence, they are ferromagnetic with the Fe.

Simultaneously Dy with the spin down configuration couples anti-ferromagnetically with Fe and Nd (Fig. 6c). 3d band in Fe may hybridize with the 5d orbital of the neighboring Nd and/or Dy. Schematic illustration of the exchange coupling and hybridization in the $\text{Nd}_2\text{Fe}_{14}\text{B}$ and $\text{Nd}_{2-x}\text{Dy}_x\text{Fe}_{14}\text{B}$ is shown in Fig. 6c.

Magnetic moment of $\text{Nd}_{2-x}\text{Dy}_x\text{Fe}_{14}\text{B}$ have been strongly affected by Dy owing to its anti-ferromagnetic coupling with Fe and Nd. Individual values of magnetic moments of $\text{Nd}_2\text{Fe}_{14}\text{B}$, $\text{Nd}_{1.75}\text{Dy}_{0.25}\text{Fe}_{14}\text{B}$ and $\text{Nd}_{1.5}\text{Dy}_{0.5}\text{Fe}_{14}\text{B}$, were determined as 25.50, 23.48, and 21.03 μB , respectively. Magnetic moments were determined by the M_s values from M–H curves (Fig. 6a). Complete M–H curves with applied magnetic field range of -9.5 to 9.5 T are provided in supplementary information as Fig. S-7. These experimentally determined values of magnetic moment are lower than the values by theoretical calculation because the theoretical parameter conditions are not fixed as the experimental ones²¹. For example, the theoretical calculation was based on the temperature at 5 K and all particles are single domain and un-oxidized. Dy coupled anti-ferromagnetically to Fe in the crystal lattice, resulting in the lower magnetic moment of $\text{Nd}_{2-x}\text{Dy}_x\text{Fe}_{14}\text{B}$. The change of magnetic moment critically affected the coercivity. From the Fig. 6 the coercivity (H_c) values of $\text{Nd}_2\text{Fe}_{14}\text{B}$, $\text{Nd}_{1.75}\text{Dy}_{0.25}\text{Fe}_{14}\text{B}$ and $\text{Nd}_{1.5}\text{Dy}_{0.5}\text{Fe}_{14}\text{B}$ were determined as 4.58, 5.84 and 9.55 kOe, respectively. $\text{Nd}_{2-x}\text{Dy}_x\text{Fe}_{14}\text{B}$ showed the higher H_c due to stronger anisotropy energy and reduced magnetic moment. Additionally, Dy substituted particles have a smaller grain size as shown in SEM results. It is well known that coercivity increases as particle size gets smaller and approaches to the single domain size. The increasing order of coercivity as $\text{Nd}_2\text{Fe}_{14}\text{B} < \text{Nd}_{1.75}\text{Dy}_{0.25}\text{Fe}_{14}\text{B} < \text{Nd}_{1.5}\text{Dy}_{0.5}\text{Fe}_{14}\text{B}$ and the decreasing order of magnetic moment as $\text{Nd}_2\text{Fe}_{14}\text{B} > \text{Nd}_{1.75}\text{Dy}_{0.25}\text{Fe}_{14}\text{B} > \text{Nd}_{1.5}\text{Dy}_{0.5}\text{Fe}_{14}\text{B}$ were obtained from M–H curves.

Energy density or energy product is the amount of energy stored in the anisotropic $\text{Nd}_2\text{Fe}_{14}\text{B}$ (or $\text{Nd}_{2-x}\text{Dy}_x\text{Fe}_{14}\text{B}$) lattice because of arrangement of the atoms in the crystal. It is confirmed that the Dy substitutions results in the higher energy density. Energy densities for $\text{Nd}_2\text{Fe}_{14}\text{B}$, $\text{Nd}_{1.75}\text{Dy}_{0.25}\text{Fe}_{14}\text{B}$ and $\text{Nd}_{1.5}\text{Dy}_{0.5}\text{Fe}_{14}\text{B}$ were recorded as 39.71, 50.29 and 53.71 kJ/m^3 , respectively. M_r (emu/g), M_s (emu/g), squareness ratio (S_q), magnetic moment (μB), coercivity (H_c), and energy density values for the all $\text{Nd}_2\text{Fe}_{14}\text{B}$ and $\text{Nd}_{2-x}\text{Dy}_x\text{Fe}_{14}\text{B}$ particles are shown in Fig. 6b, comparatively. M–H curve with S.I. units of coercivity (kA/m) is provided in supplementary information as Fig. S8.

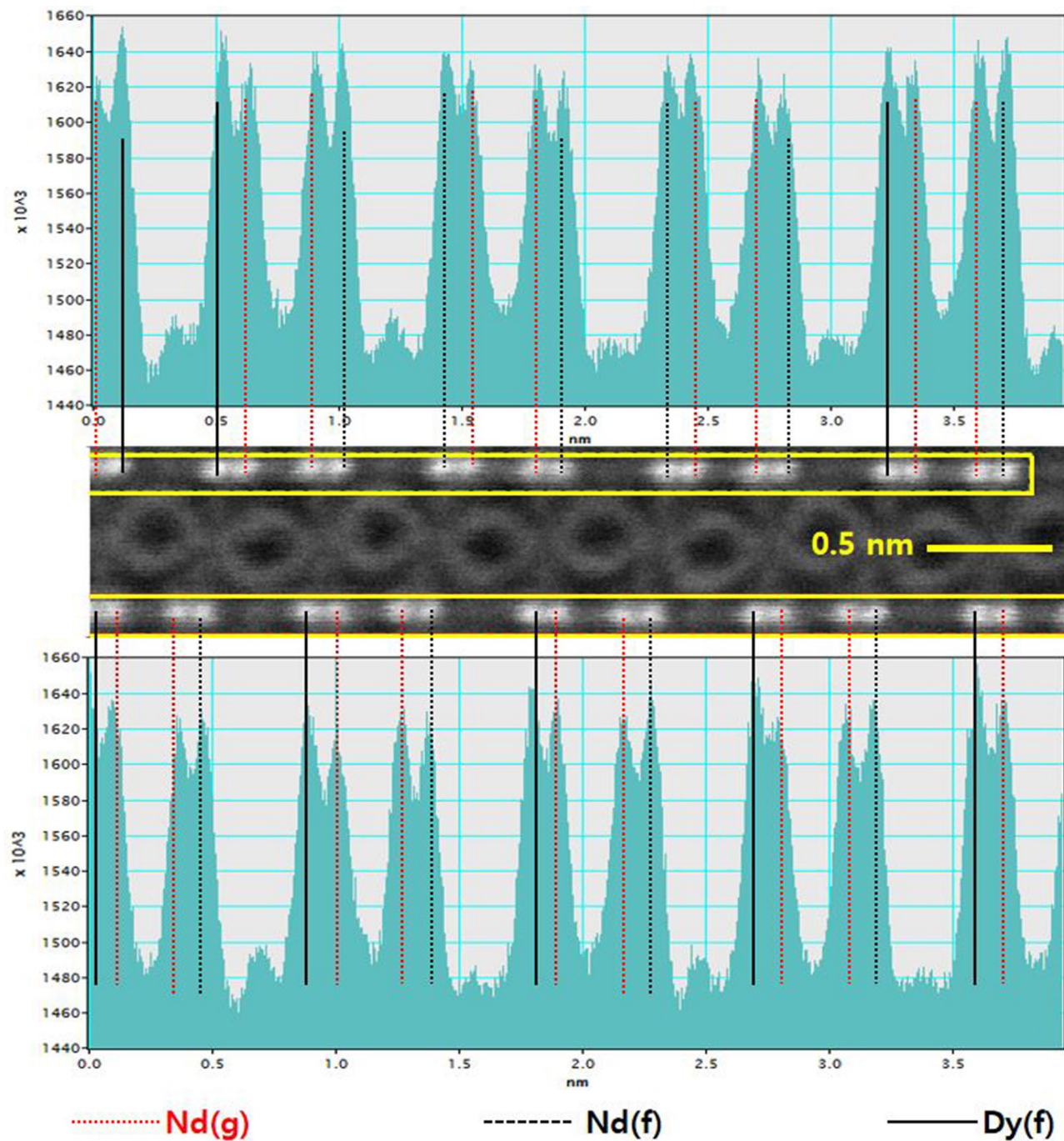


Figure 5. HADDF-STEM image of $\text{Nd}_{1.5}\text{Dy}_{0.5}\text{Fe}_{14}\text{B}$ at [100] zone axis, with intensity histogram. Light grey circles in the center indicate Fe atoms.

$\text{Nd}_2\text{Fe}_{14}\text{B}$ and $\text{Nd}_{2-x}\text{Dy}_x\text{Fe}_{14}\text{B}$ are expected to be anisotropic, hence, magnetic moment and energy density are angular dependent magnetic properties. Closely packed particles of $\text{Nd}_2\text{Fe}_{14}\text{B}$ and $\text{Nd}_{2-x}\text{Dy}_x\text{Fe}_{14}\text{B}$ were aligned at 5 T with easy direction of magnetization, then magnetic field was reduced to the 200 Oe. Thereafter, sample was rotated in the angle range of 0° – 180° . Figure 7a explains the preparation of the sample for the measurement of magnetic anisotropy. During the measurement at MPMS, the magnetic particles were closely packed, which stopped the rotation of the particles at low applied magnetic field (200 Oe). All processes were performed at room temperature so that the effect of thermal energy was neglected.

Figure 7b shows the anisotropic character of the $\text{Nd}_2\text{Fe}_{14}\text{B}$ and $\text{Nd}_{2-x}\text{Dy}_x\text{Fe}_{14}\text{B}$. When magnetic particles were rotated in the range of 0° – 180° at constant applied magnetic field of 200 Oe, magnetic moment of the particles was changed significantly. $\text{Nd}_2\text{Fe}_{14}\text{B}$ and $\text{Nd}_{2-x}\text{Dy}_x\text{Fe}_{14}\text{B}$ have maximum magnetic moment along “c” crystal direction, with parallel/anti-parallel orientation to the applied field of ($\theta=0^\circ$, 180°). This is because of the “c” crystal dimension is easy direction for magnetization. On the contrary, along “a” and “b” crystal direction magnetic moment approached to zero.

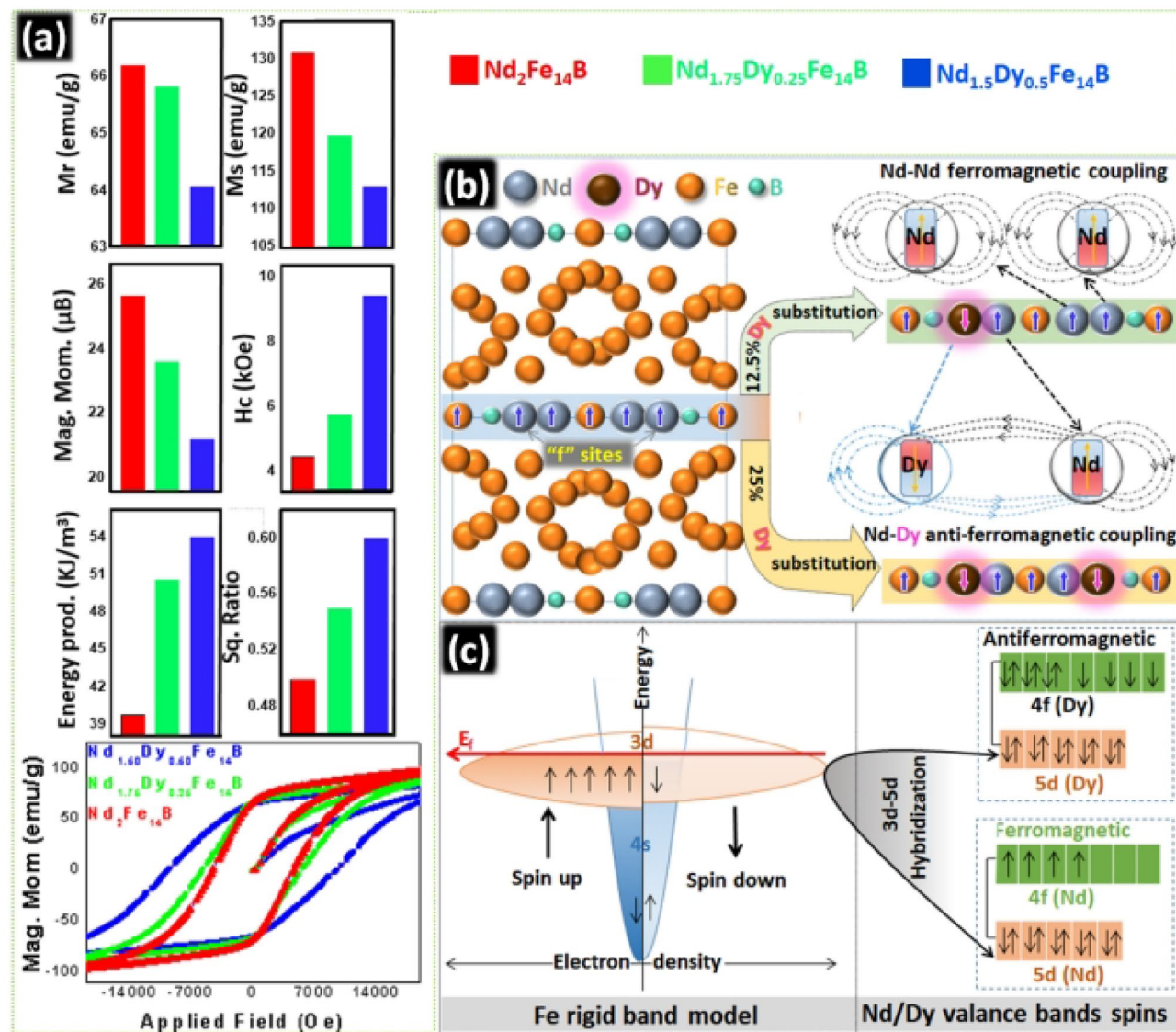


Figure 6. (a) M–H curves, M_r , M_s , Magnetic moment, H_c , energy density and squareness ratio of $\text{Nd}_2\text{Fe}_{14}\text{B}$, $\text{Nd}_{1.75}\text{Dy}_{0.25}\text{Fe}_{14}\text{B}$ and $\text{Nd}_{1.5}\text{Dy}_{0.5}\text{Fe}_{14}\text{B}$ particles. (b) Schematic illustration to explain the ferro and anti-ferromagnetic coupling between Nd, Dy and Fe (c) Explanation of coupling and hybridization between Nd, Dy and Fe.

Maximum magnetic moment value (24.13 μB) of $\text{Nd}_2\text{Fe}_{14}\text{B}$ obtained during rotation was lower than the magnetic moment values obtained from M–H curves (25.50 μB). Reduced value of magnetic moment was observed because of weak applied magnetic field (200 Oe) during the rotation of the magnetic particles. However, the trend of magnetic moment variation for both the $\text{Nd}_2\text{Fe}_{14}\text{B}$ and $\text{Nd}_{2-x}\text{Dy}_x\text{Fe}_{14}\text{B}$ was same. Conclusively, substitution of Dy for Nd does not affect the anisotropic patterns of the crystal, however, value of the energy density can be changed. Figure S-8 explains the interaction of the applied magnetic field and the electron spin density of $\text{Nd}_2\text{Fe}_{14}\text{B}$ during the rotation.

Magnetic moments of $\text{Nd}_2\text{Fe}_{14}\text{B}$, $\text{Nd}_{2-x}\text{Dy}_x\text{Fe}_{14}\text{B}$ and Nd were calculated theoretically by full potential linearized augmented plane wave method, as implemented in the Wien2k code. Individual magnetic moments of Nd and Dy atoms at different sites were also calculated theoretically by this method. Theoretically calculated magnetic moment values for $\text{Nd}_2\text{Fe}_{14}\text{B}$, Nd (f) and Nd (g) were 30.20, 3.32 3.30 μB , respectively. Experimentally determined values for the $\text{Nd}_2\text{Fe}_{14}\text{B}$, Nd (f) Nd (g) were 24.3, 2.69, 2.67 μB , respectively. Details of experimental and theoretical calculations are provided in the “supplementary information”.

Theoretically Nd always occupies the “g” site in $\text{Nd}_2\text{Fe}_{14}\text{B}$, $\text{Nd}_{1.75}\text{Dy}_{0.25}\text{Fe}_{14}\text{B}$ and $\text{Nd}_{1.5}\text{Dy}_{0.5}\text{Fe}_{14}\text{B}$ ^{19–21}. This is also confirmed in this work (Fig. 4). Hence in case of $\text{Nd}_{1.75}\text{Dy}_{0.25}\text{Fe}_{14}\text{B}$ and $\text{Nd}_{1.5}\text{Dy}_{0.5}\text{Fe}_{14}\text{B}$ there is negligible change in the magnetic moment on the “g” site after substitution. In $\text{Nd}_2\text{Fe}_{14}\text{B}$ formula unit, Nd is distributed equally among 50% “f” and 50% “g” sites. Magnetic moment on “f” and “g” sites of in $\text{Nd}_2\text{Fe}_{14}\text{B}$ is determined as 2.69 and 2.67 μB , respectively.

In $\text{Nd}_{1.75}\text{Dy}_{0.25}\text{Fe}_{14}\text{B}$ and $\text{Nd}_{1.5}\text{Dy}_{0.5}\text{Fe}_{14}\text{B}$, Nd occupies 75% and 50% “f” sites, simultaneously Dy occupies leftover 25% and 50% “f” sites respectively. Hence magnetic moment on one “f” sites in $\text{Nd}_{1.75}\text{Dy}_{0.25}\text{Fe}_{14}\text{B}$ and

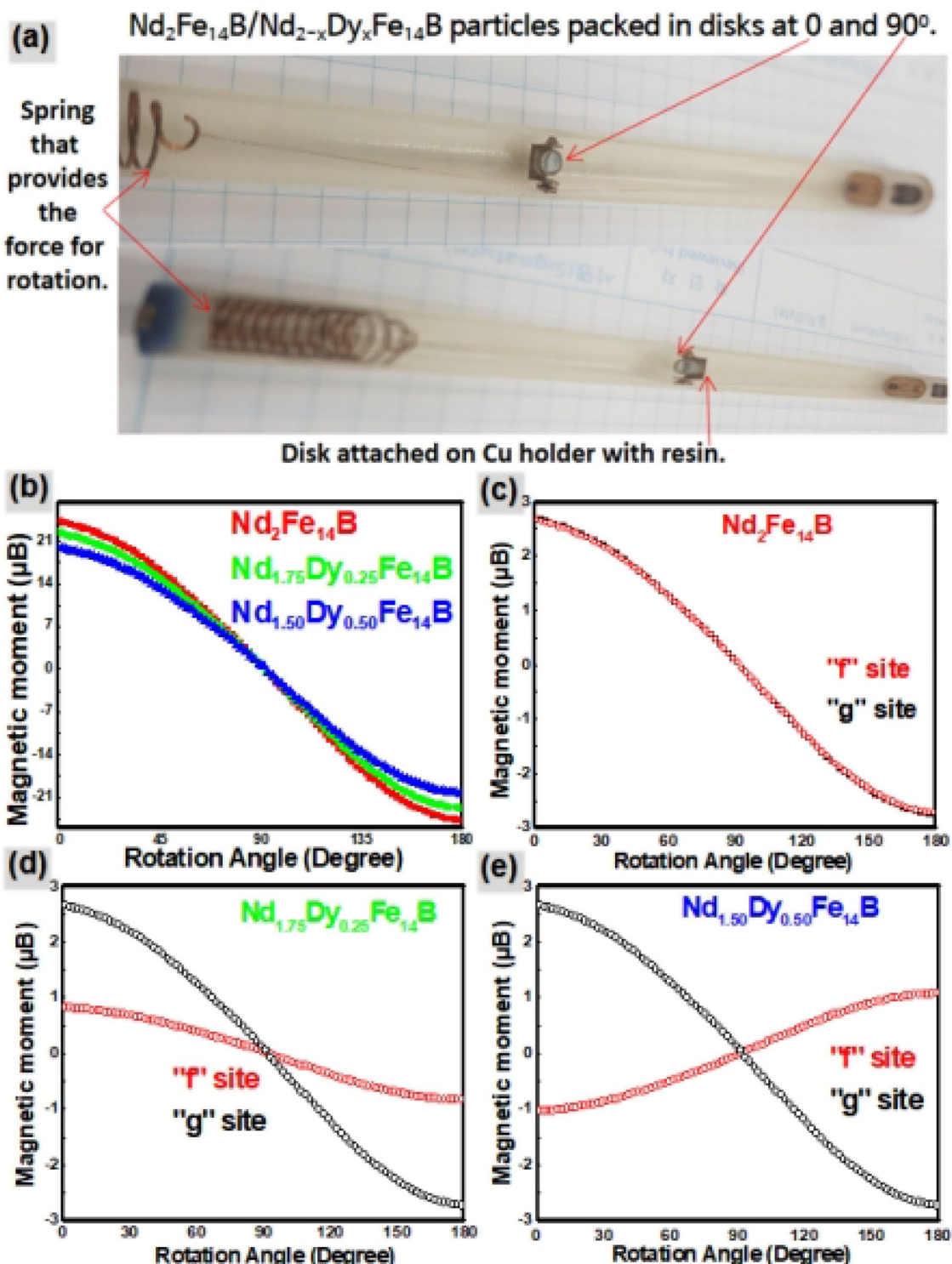


Figure 7. (a) Sample preparation for the measurement of magnetic anisotropy (b) Magnetic moment of Nd₂Fe₁₄B, Nd_{1.75}Dy_{0.25}Fe₁₄B and Nd_{1.5}Dy_{0.5}Fe₁₄B particles as a function of rotation angle. Magnetic moment at the "f" and "g" sites in (c) Nd₂Fe₁₄B (d) Nd_{1.5}Dy_{0.5}Fe₁₄B (e) Nd_{1.75}Dy_{0.25}Fe₁₄B as a function of rotation angle.

Nd_{1.5}Dy_{0.5}Fe₁₄B was determined as 0.82 and $-1.05\ \mu\text{B}$, respectively. Dy, which has almost double magnetic moment ($5.34\ \mu\text{B}$) as compared to the Nd ($2.45\ \mu\text{B}$), reduces the magnetic moment very effectively after the substitution. Reduction of magnetic moment of in the Nd_{2-x}Dy_xFe₁₄B formula unit is actually the reduction of the magnetic moment of the "f" site.

After obtaining the experimental values of the magnetic moments of the Nd₂Fe₁₄B, Nd (f) and Nd (g), anisotropic behavior of "f" and "g" sites was studied. Figure 7a explains the sample preparation for the measurement

Substitution sites	Magnetic moment (μB)		
	$\text{Nd}_2\text{Fe}_{14}\text{B}$	$\text{Nd}_{1.75}\text{Dy}_{0.25}\text{Fe}_{14}\text{B}$	$\text{Nd}_{1.50}\text{Dy}_{0.50}\text{Fe}_{14}\text{B}$
f sites (0°)	2.69	0.82	-1.05
f sites (180°)	-2.71	-0.85	1.06
g sites (0°)	2.67	2.67	2.67
g sites (180°)	-2.71	-2.71	-2.71

Table 1. Magnetic moment values of $\text{Nd}_2\text{Fe}_{14}\text{B}$ and $\text{Nd}_{2-x}\text{Dy}_x\text{Fe}_{14}\text{B}$ at “f” and “g” sites at rotating angle of 0° and 180°.

of magnetic anisotropy. $\text{Nd}_2\text{Fe}_{14}\text{B}$, and $\text{Nd}_{1.75}\text{Dy}_{0.25}\text{Fe}_{14}\text{B}$ particles were compressed in the plastic discs and then attached to the rotating plate with the resin. Wires and springs used in the apparatus are made of Cu, which is non-magnetic. When these samples were kept in the MPMS they were rotated by application of force on the spring. Magnetic moment values of the “f” and “g” sites in $\text{Nd}_2\text{Fe}_{14}\text{B}$ and $\text{Nd}_{2-x}\text{Dy}_x\text{Fe}_{14}\text{B}$ at various angles of rotation are given in the Table 1. Figure 7b graphically illustrates that the magnetic moment of $\text{Nd}_2\text{Fe}_{14}\text{B}$ and $\text{Nd}_{2-x}\text{Dy}_x\text{Fe}_{14}\text{B}$ as the function of rotating angle in the constant magnetic field. Figure 7c–e shows the variation of individual magnetic moments of “f” and “g” sites as the function of rotating angle.

Conclusions

$\text{Nd}_2\text{Fe}_{14}\text{B}$ and $\text{Nd}_{2-x}\text{Dy}_x\text{Fe}_{14}\text{B}$ ($x=0.25, 0.50$) particles were successfully prepared by the modified co-precipitation method followed by reduction–diffusion process. Micro-structure analysis of the composition and distribution of elements confirmed the homogeneous distribution of Dy atoms in the crystal lattice of $\text{Nd}_2\text{Fe}_{14}\text{B}$ and Dy substitution at “4-f” site. Orbital magnetic moment (L) direction of the unpaired valence electrons of Dy was opposite to the Fe and Nd which resulted in the anti-ferromagnetic coupling between them. Nd substitution with Dy on “f” site reduced the magnetic moment of $\text{Nd}_2\text{Dy}_x\text{Fe}_{14}\text{B}$ due to anti-ferromagnetic coupling with Nd and Fe, but enhanced the energy density, squareness ratio and coercivity. Furthermore, it was found that $\text{Nd}_2\text{Fe}_{14}\text{B}$ and $\text{Nd}_{2-x}\text{Dy}_x\text{Fe}_{14}\text{B}$ particles have maximum magnetic moment when they are aligned parallel or anti-parallel to the applied magnetic field and have the minimum energy density when they are rotated perpendicular to the applied magnetic field. Conclusively, “f” site substitution of Nd with Dy in $\text{Nd}_2\text{Fe}_{14}\text{B}$ did not change the anisotropic patterns of $\text{Nd}_{2-x}\text{Dy}_x\text{Fe}_{14}\text{B}$.

Received: 18 January 2021; Accepted: 1 March 2021

Published online: 18 March 2021

References

1. Muljadia, M. & Sardjonoa, P. Preparation and characterization of 5 wt% epoxy resin bonded magnet NdFeB for micro generator application. *Supraped. Ener. Proced.* **68**, 282–287. <https://doi.org/10.1016/j.egypro.2015.03.257> (2015).
2. Honshima, M. & Ohashi, K. High-energy NdFeB agnets and their applications. *J. Mat. Engg. Perform.* **3**(2), 218–222. <https://doi.org/10.1007/BF02645846> (1994).
3. Ma, X. H. *et al.* Preparation of Nd–Fe–B by nitrate–citrate auto-combustion followed by the reduction–diffusion process. *Nanoscale* **7**, 8016–8022. <https://doi.org/10.1039/C5NR01195G> (2015).
4. Jeong, H. *et al.* Chemical synthesis of $\text{Nd}_2\text{Fe}_{14}\text{B}$ hard phase magnetic nanoparticles with an enhanced coercivity value: Effect of CaH_2 amount on the magnetic properties. *N. J. Chem.* **40**, 10181. <https://doi.org/10.1039/C6NJ02436J> (2016).
5. Kim, C. W., Kim, Y. H., Pal, U. & Kang, Y. S. Facile synthesis and magnetic phase transformation of Nd–Fe–B nanoclusters by oxygen bridging. *J. Mater. Chem. C* **1**, 27. <https://doi.org/10.1039/C2TC00083K> (2013).
6. Amirouche, F., Zhou, Y. & Johnson, T. Current micro pump technologies and their biomedical applications. *Microsyst. Technol.* **15**, 647–666. <https://doi.org/10.1007/s00542-009-0804-7> (2009).
7. Chen, Z., Miller, D. & Herchenroeder, J. High performance nanostructured Nd–Fe–B fine powder prepared by melt spinning and jet milling. *J. Appl. Phys.* **107**, 09A730.1–09A730.4. <https://doi.org/10.1063/1.3348544> (2010).
8. Riaño, S. & Binnemans, K. Extraction and separation of neodymium and dysprosium from used NdFeB magnets: An application of ionic liquids in solvent extraction towards the recycling of magnets. *Green Chem.* **17**, 2931–2942. <https://doi.org/10.1039/C5GC00230C> (2015).
9. Reimer, M. V., Schenk-Mathes, H. Y., Hoffmann, M. F. & Elwert, F. Recycling decisions in 2020, 2030, and 2040, when can substantial NdFeB extraction be expected in the EU?. *Metals* **8**, 867.1–867.5. <https://doi.org/10.3390/met8110867> (2018).
10. Cha, H. G., Kim, Y. H., Kim, C. W. & Kang, Y. S. Preparation for exchange-coupled permanent magnetic composite between α -Fe (soft) and $\text{Nd}_2\text{Fe}_{14}\text{B}$ (hard). *Curr. Appl. Phys.* **7**(4), 400–403. <https://doi.org/10.1016/j.cap.2006.09.010> (2007).
11. Akiya, T., Kato, H., Sagawa, M. & Koyama, K. Enhancement of coercivity in Al and Cu added Nd–Fe–B sintered magnets by high field annealing. *IOP Conf. Series Mat. Sci. Eng.* **012034**(1–012034), 7. <https://doi.org/10.1088/1757-8981/1/1/012034> (2009).
12. Yu, N. J., Pan, N. J., Zhang, P. Y. & Ge, H. L. The origin of coercivity enhancement of sintered NdFeB magnets prepared by Dy addition. *J. Magnet.* **18**(3), 235–239. <https://doi.org/10.4238/JMAG.2013.18.3.235> (2013).
13. Li, W. F., Sepehri-Amin, H., Ohkubo, T., Hase, N. & Hono, K. Distribution of Dy in high-coercivity (Nd, Dy)–Fe–B sintered magnet. *Acta Mater.* **59**, 3061–3069. <https://doi.org/10.1016/j.actamat.2011.01.046> (2011).
14. Tan, X., Parmar, X., Zhong, Y., Chaudhary, V. & Ramanujan, R. V. Effect of Dy substitution on the microstructure and magnetic properties of high (BH)_{max} Nd–Dy–Fe–Co–B nanoparticles prepared by microwave processing. *J. Magn. Magn. Mater.* **471**, 278–285. <https://doi.org/10.1016/j.jmmm.2018.09.017> (2019).
15. Wenlong, Y. *et al.* Influence of gadolinium on microstructure and magnetic properties of sintered NdGdFeB magnets. *J. Rare Earth.* **30**, 133–136. [https://doi.org/10.1016/S1002-0721\(12\)60009-X](https://doi.org/10.1016/S1002-0721(12)60009-X) (2012).

16. Zhong, Y., Chaudhary, V., Tan, X., Parmar, H. & Ramanujan, R. V. High coercivity Dy substituted Nd-Fe-Co-B magnetic nanoparticles produced by mechanochemical processing. *Magn. Magn. Mater.* **475**, 554–562. <https://doi.org/10.1016/j.jmmm.2018.08.061> (2019).
17. Rahimi, H., Ghasemi, A., Mozaffarinia, R. & Tavoosi, M. Coercivity enhancement mechanism in Dy-substituted Nd-Fe-B nanoparticles synthesized by sol-gel base method followed by a reduction diffusion process. *J. Magn. Magn. Mater.* **429**, 182–191. <https://doi.org/10.1016/j.jmmm.2017.01.041> (2017).
18. Khan, I. & Hong, J. Electronic structure and magnetic properties of $\text{Nd}_2\text{Fe}_{14}\text{B}$. *J. Kor. Phys. Soc.* **68**, 1409–1414. <https://doi.org/10.3938/jkps.68.1409> (2016).
19. Alam, A., Khan, M., McCallum, R. W. & Johnson, D. D. Site-preference and valency for rare-earth sites in $(\text{R}-\text{Ce})_2\text{Fe}_{14}\text{B}$ magnets. *Appl. Phys. Lett.* **102**, 042402.1–042402.5. <https://doi.org/10.1063/1.4789527> (2013).
20. Kitagawa, I. & Asari, Y. Magnetic anisotropy of $\text{R}_2\text{Fe}_{14}\text{B}$ ($\text{R}=\text{Nd}, \text{Gd}, \text{Y}$): Density functional calculation by using the linear combination of pseudo-atomic-orbital method. *Phys. Rev. B* **81**, 214408.1–214408.7. <https://doi.org/10.1103/PhysRevB.81.214408> (2010).
21. Liu, X. B. & Altounian, Z. The partitioning of Dy and Tb in NdFeB magnets: A first-principles study. *J. Appl. Phys.* **111**, 07A701.1–07A701.3. <https://doi.org/10.1063/1.3670054> (2012).
22. Itakura, M., Watanabe, N., Nishida, M., Daio, T. & Matsumura, S. Atomic-resolution X-ray energy-dispersive spectroscopy chemical mapping of substitutional Dy atoms in a high-coercivity neodymium magnet. *Jap. J. App. Phys.* **52**, 050201. <https://doi.org/10.7567/JJAP.52.050201> (2013).
23. Saito, K., Doi, S., Abe, T. & Ono, K. Quantitative evaluation of site preference in Dy-substituted $\text{Nd}_2\text{Fe}_{14}\text{B}$. *J. Alloy. Comd.* **721**, 476–481. <https://doi.org/10.1016/j.jallcom.2017.04.155> (2017).
24. Ma, Z., Zhang, T. & Jiang, C. A facile synthesis of high performance SmCo_5 nanoparticles. *Chem. Eng. J.* **264**, 610–616. <https://doi.org/10.1016/j.cej.2014.11.138> (2015).
25. Palaka, S. *et al.* A facile chemical synthesis of PrCo_5 particles with high performance. *J. Alloy. Comd.* **812**, 151674. <https://doi.org/10.1016/j.jallcom.2019.151674> (2020).
26. Kim, T. A., Kang, M. C., Jung, G. B., Kim, D. S. & Yang, C. W. Novel method for preparing transmission electron microscopy samples of micrometer-sized powder particles by using focused ion beam. *Microsc. Microanal.* **23**, 1055–1060. <https://doi.org/10.1017/S1431927617012557> (2017).
27. Syed, K. H., Jin-Young, L., Dongsoo, K. & Kang, Y. S. Eco-friendly facile three-step recycling method of $(\text{Nd}-\text{RE})_2\text{Fe}_{14}\text{B}$ magnet sludge and enhancement of $(\text{BH})_{\text{max}}$ by ball milling in ethanol. *ACS Sustain. Chem. Eng.* **8**, 8156–8163. <https://doi.org/10.1021/acssuschemeng.0c00584> (2020).
28. Cullity, B. D. *Elements of X-ray Diffraction* 340–341 (Addison-Wesley, 1956).
29. Charbel, T. Crystal structure, X-ray diffraction and Oblique geometry: Volumes, distances and angles. *Eur. J. Phys.* **2**, 1–10 (2019).
30. Herbst, J. F., Croat, J. F., Pinkerton, F. E. & Yelon, W. B. Relationships between crystal structure and magnetic properties in $\text{Nd}_2\text{Fe}_{14}\text{B}$. *Phys. Rev. B* **29**, 1–4. <https://doi.org/10.1103/PhysRevB.29.4176> (1984).

Acknowledgements

This work was supported by a National Research Council of Science and Technology (NST) grant by the Korea government (MSIT) (No. CRC-15-06-KIGAM). Y.S. Kang also appreciate for the financial support by the Leader Project at the Sogang University funded by the Ministry of Science and ICT through the National Research Foundation of Korea (No. 2020R1A3B3079715).

Author contributions

S.K.H. performed experiment did characterization and wrote manuscript. Y.S.K. helped in data interpretation and manuscript writing. D.K. helped in experiment and characterization. C.-W.Y. and M.-C.K. did the characterization for structural analysis and helped in the data interpretation and figures making. J.H. provided simulation data for the magnetic moment.

Competing interests

The authors declare no competing interests.

Additional information

Supplementary Information The online version contains supplementary material available at <https://doi.org/10.1038/s41598-021-85713-5>.

Correspondence and requests for materials should be addressed to Y.S.K., C.-W.Y. or D.K.

Reprints and permissions information is available at www.nature.com/reprints.

Publisher's note Springer Nature remains neutral with regard to jurisdictional claims in published maps and institutional affiliations.



Open Access This article is licensed under a Creative Commons Attribution 4.0 International License, which permits use, sharing, adaptation, distribution and reproduction in any medium or format, as long as you give appropriate credit to the original author(s) and the source, provide a link to the Creative Commons licence, and indicate if changes were made. The images or other third party material in this article are included in the article's Creative Commons licence, unless indicated otherwise in a credit line to the material. If material is not included in the article's Creative Commons licence and your intended use is not permitted by statutory regulation or exceeds the permitted use, you will need to obtain permission directly from the copyright holder. To view a copy of this licence, visit <http://creativecommons.org/licenses/by/4.0/>.

© The Author(s) 2021